Characterization and Simulation of an Adaptable Fan-Beam Collimator for Fast Calibration of Radiation Detectors for PET

Ronja Hetzel, Florian Mueller, *Graduate Student Member, IEEE*, Jan Grahe, Axel Honné, David Schug, *Graduate Student Member, IEEE*, and Volkmar Schulz, *Member, IEEE*

***Abstract*—Monolithic scintillators for positron emission tomography systems perform best when calibrated individually. We present a fan-beam collimator with which a crystal can be calibrated within less than 1 h when suitable positioning algorithms are applied. The collimator is manufactured from lead, features an easily adaptable slit to tune the beam width and can be operated together with a coincidence detector to select a clean sample of 511-keV annihilation photons. We evaluated the performance of the collimator with a Geant4 simulation for slit widths of 0.25 mm, 0.4 mm, and 1 mm and validated the shape of the beam profile experimentally by step-wisely moving a detector into the beam. This shows a clear narrow and box-shaped beam profile even if the collimator is operated without the coincidence set-up. In the latter configuration, the fraction of gammas in the beam region on a $50\times50\,\text{mm}^2$ large detector is between 48% and 79% which is improved significantly to more than 94% by using only coincidence events. Analyzing the energy distribution shows that the fraction of 511-keV photons is increased from less than 50% to more than 96% by selecting coincidences. This demonstrates that our collimator produces a very defined and clean beam and provides optimal conditions for calibration.**

***Index Terms*—Calibration, fan-beam collimator, Geant4, monolithic scintillator, Monte Carlo simulations, positron emission tomography (PET), scintillators.**

Manuscript received December 6, 2019; revised March 10, 2020; accepted April 1, 2020. Date of publication April 28, 2020; date of current version September 2, 2020. This work was supported in part by the Interdisciplinary Centre for Clinical Research within the faculty of Medicine at the RWTH Aachen University under Grant AP1-7, and in part by the German Research Foundation (DFG) under Project 288267690. *(Ronja Hetzel and Florian Mueller contributed equally to this work.) (Corresponding authors: Ronja Hetzel; Florian Mueller.)*

Ronja Hetzel is with the Department of Physics of Molecular Imaging Systems, Institute for Experimental Molecular Imaging, RWTH Aachen University, 52074 Aachen, Germany, and also with the Physics Institute III B, RWTH Aachen University, 52074 Aachen, Germany (e-mail: ronja.hetzel@pmi.rwth-aachen.de).

Florian Mueller is with the Department of Physics of Molecular Imaging Systems, Institute for Experimental Molecular Imaging, RWTH Aachen University, 52074 Aachen, Germany (e-mail: florian.mueller@pmi.rwth-aachen.de).

Jan Grahe is with the Department of Physics of Molecular Imaging Systems, Institute for Experimental Molecular Imaging, RWTH Aachen University, 52074 Aachen, Germany, and also with the Philips Research, Department Oncology Solutions, 5656 AE Eindhoven, The Netherlands.

Axel Honné is with the Scientific Workshop, University Hospital Aachen, RWTH Aachen University, 52074 Aachen, Germany.

David Schug is with the Department of Physics of Molecular Imaging Systems, Institute for Experimental Molecular Imaging, RWTH Aachen University, 52074 Aachen, Germany, and also with the Hyperion Hybrid Imaging Systems GmbH, 52074 Aachen, Germany.

Volkmar Schulz is with the Department of Physics of Molecular Imaging Systems, Institute for Experimental Molecular Imaging, RWTH Aachen University, 52074 Aachen, Germany, also with the Hyperion Hybrid Imaging Systems GmbH, 52074 Aachen, Germany, also with the Fraunhofer MEVIS, Institute for Digital Medicine, 28359 Bremen, Germany, and also with the Physics Institute III B, RWTH Aachen University, 52074 Aachen, Germany.

Color versions of one or more of the figures in this article are available online at http://ieeexplore.ieee.org.

Digital Object Identifier 10.1109/TRPMS.2020.2990651

I. Introduction

POSITRON emission tomography (PET) is a tracer-based functional imaging technique which has found broad applications in research and clinical praxis [1], [2]. An arrangement of radiation detectors registers the two 511 keV gamma photons created by the annihilation of the tracer's β^+ decay. PET detectors usually consist of an anorganic scintillator (e.g., BGO, LSO, and LYSO) converting the gamma photons to optical photons and a multichannel photosensor array [3]–[5].

Radiation detectors based on monolithic scintillation crystals are an attractive alternative to segmented detector concepts. Monolithic crystals provide good spatial, energy, and timing resolution [6]–[12]. Furthermore, these detectors have intrinsic depth-of-interaction (DOI) capabilities [13]–[16]. DOI information reduce the parallax error at off-center positions within a PET ring (radial astigmatism) [17], especially important for preclinical or organ-dedicated applications [18]. While preclinical scanners based on DOI-capable monolithic detectors are already available [19], [20], most current whole-body scanner employ segmented detector designs without DOI [21]. One of the main challenges to widely translate monolithic scintillators to both preclinical and clinical application are efficient calibration routines and positioning algorithms.

Position estimation in monolithic scintillators can be divided up into two groups: 1) parametric and 2) statistical models. Parametric methods analytically model the position-dependency of the light distribution inside the scintillation crystal [22], [23]. These models often show a decreased positioning performance toward the scintillator's edges due to light truncation [22] or might be affected by imperfections of the detector. Statistical approaches rely on training data consisting of measured light distributions with known reference positions. Several statistical methods have been presented in literature, e.g., k-nearest neighbors (kNNs) [24], neural networks [8], [25], [26], maximum likelihood [27], Voronoi

diagrams [28], and gradient tree boosting [11], [14]. To obtain a suitable training data set, the reference position of gamma photons should be known as precise as possible. Furthermore, wrongly labeled gamma interactions should be reduced to a minimum. Both goals can be achieved with a collimated beam of gamma photons of the controlled beam profile.

Multiple methods to collimate gamma photons have been used in literature: the most simple method is electronic collimation as no further instrumentation except PET components is needed [29], [30]. However, the beam profile depends on the accuracy the coincidence detector achieves. An alternative approach is dedicated setups shaping a gamma beam usually consisting of a material with high atomic mass (e.g., tungsten or lead). First, parallel hole collimators with precise drilling of known diameter ranging from 0.5 mm to 1.0 mm were employed for PET detector calibration [9], [24], [25], [27], [31]. The thickness of the shielding material and shape of the parallel hole determine the beam profile. However, parallel hole collimators suffer from a low count rate due to the shrunk solid angel. Positioning calibrations of monolithic scintillators based on parallel hole collimators can last up to the order of weeks [24] which seems impractical for the use for large-scale PET systems. Later, fan-beam collimators were proposed for calibration. The approach was tested through simulation and experiment for the kNNs algorithm [24], [32]. The positioning calibration of a fan-beam collimator is strictly 1-D. Thus, two calibrations for both planar directions need to be performed. It was shown that a few thousand events per irradiation position lead to good positioning results [32], [33]. With this, the fan-beam collimator enabled a detector calibration within the order of hours (equals a speed-up of factor 20). Recently, we presented a gradient tree boosting-based algorithm for planar and DOI positioning utilizing fan-beam collimated training data lasting less than 1 h [11], [14].

Here, we present the detailed concept of the employed fan-beam collimator. The collimator is simple to manufacture and has an easily adaptable beam width which spreads over 50 mm for both the detector under test and the coincidence detector. The collimator is simulated in Geant4 to study the unadulterated beam and parameters which are not easily accessible in a measurement. We investigate the fraction of gamma photons inside the beam and the energy distributions. The beam profile is then experimentally validated.

II. Materials

A. Fan-Beam Collimator

The fan-beam collimator consists of a bottom shielding, a top shielding, a source holder, and two shielding cakes (see Fig. 1 side view). The shielding cakes create a finite slit which can be independently adjusted. The gamma photons of up to two β^+ emitter sources exit the collimator through the created slits. A coincidence detector and detector under test are placed in front of the beam slits. Fig. 1 top view illustrates the resulting beams. The fan beam is shrunk in width by the bottom shielding and top shielding to the sides. Also, both bottom and top shielding reduce the gamma activity

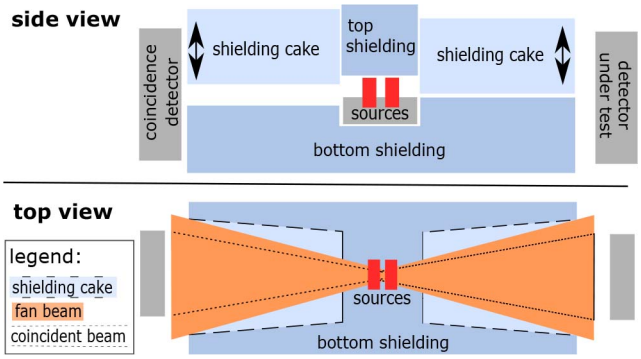

Fig. 1. Design principle of the fan-beam collimator. Side view: Bottom shielding and shielding cakes define the beam width. Top view: The shape of the shielding cakes restrict the span of the fan beam. The coincidence detector determines the coincident area of the beam. Reprinted from [11], CC3.0.

to the environment. The coincidence detector determines the coincident beam. To avoid a loss of coincidences by geometric effects or manufacturing uncertainties, the coincidence detector is placed closer to the collimator than the detector under test. Furthermore, the slit width of the coincidence detector was chosen to be larger than the other one.

The design of the fan-beam collimator is based on two standard lead blocks with dimensions of 200 mm $\times$ 100 mm $\times$ 50 mm, which makes it easy to fabricate. The mechanical realization of the fan-beam collimator is displayed in Fig. 2(a). The whole fan-beam collimator was manufactured out of the lead blocks employing a CNC milling machine. All outer surfaces of the lead elements are covered with a self-gluing plastic foil to reduce contact with human skin. Dedicated handles for both top shielding and shielding cakes allow easy handling of the devices. To maintain the distance between bottom shielding and cakes, each cake is equipped with four screws positioned outside the direct beam path to minimize Compton scattering of gamma photons in the beam path. Each screw provides a metric fine pitch thread of 0.5 mm/turn and a variable excess length between 0 mm and 14 mm. A dial indicator of 0.01 mm precision was used to determine the excess length. The beam spans 50 mm exiting the lead block defined by the geometrical shape of the collimator.

In addition, the mechanical realization provides a dedicated source alignment tool for two disk sources of 32.6 mm [see Fig. 2(b)]. To achieve the optimal coincidence rate, the radioactive area of both equipped sources should be in the middle plane of the detector under study's beam slit. Thus, the sources need to be variable in height which is realized by four screws with fine pitch thread. As observed in our lab, the radioactive area may be located slightly off-center within the disk. Therefore, the source alignment tool allows an individual offset of every source. Together with the rotation of the disks, the radioactive areas can be aligned to one plane. A further screw allows for slight fixation of the disks. Here, the source alignment tool hosts up to two sources, while the concept can be adapted to multiple sources. So several sources can be combined to increase the overall activity. We used ^{22}Na sources as they are commonly available in physical laboratories.

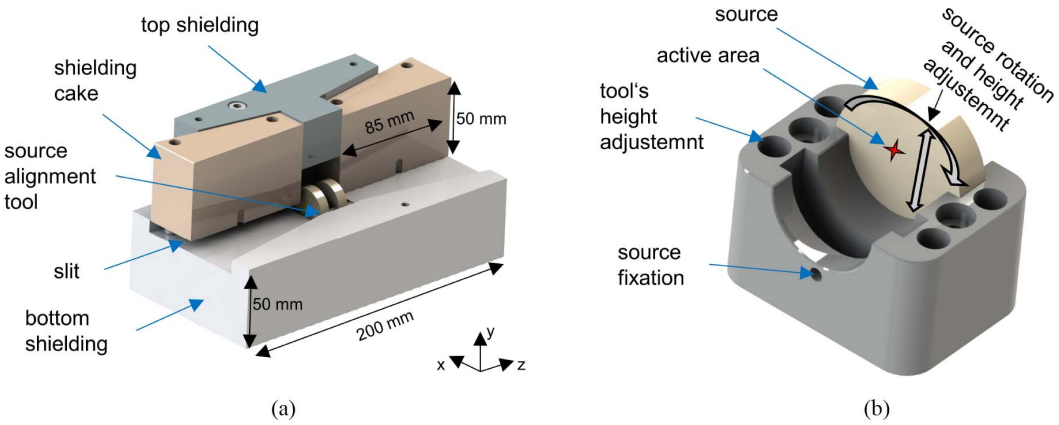

Fig. 2. (a) Section view of the fan-beam collimator. Four screws maintain the distance between bottom shielding and shielding cakes. The top shielding reduces scatter events and shields the sources. (b) Source alignment tool. The tool hosts up to two sources. The radioactive area of the sources can be aligned to one plane by individual rotation and height adjustment of the sources. The whole source alignment tool can be shifted in height as well to adapt for different beam widths.

B. Geant4 Simulation

The collimator was simulated in Geant4 10.04.p02 to study the beam profile and energy distribution [34]. The used PhysicsLists were G4DecayPhysics and G4EmStandardPhysics_option4 as recommended for medical purposes. The collimator was simulated as composed of the top and bottom shielding, the two shielding cakes, the brass screws for the slit adjustment and the source holder, analog to the design depicted in Fig. 2(a). The two sources consisted of NaCl where all sodium was replaced by ^{22}Na. They had a spherical shape with a diameter of 0.5 mm and are embedded in cylindrical capsules made of PMMA. The capsules were placed in the source holder so that the sources were centered with respect to the slit toward the detector under test. The coincidence detector was represented by a monolithic LYSO crystal of 100 mm $\times$ 100 mm $\times$ 19 mm. It was placed 12 mm behind the collimator. The perpendicular dimensions were set larger than necessary to minimize the influence to the beam profile. The distance and thickness of the detector were chosen to match the experimental conditions of the validation measurement in our lab. The total energy deposited in this detector was recorded for the analysis. There was no detector under test included in the simulation. Instead, virtual planes were defined at 1 mm, 5 mm, 10 mm, 11 mm, 30 mm, 34 mm, 40 mm, and 50 mm in front of the collimator to track the path of the gamma photons. As the collimator was designed for detector sizes of up to 50 mm, the dimension of the virtual planes is set to 50 mm $\times$ 50 mm. If a gamma photon crossed any of these planes, its current positions and energy were stored.

To study the performance of the collimator, three different slit widths were investigated. We chose slits of 0.25 mm, 0.4 mm, and 1 mm exemplarily as they are typically used for calibration in our lab. The slit toward the coincidence detector was set to 5 mm for all three set-ups. For each configuration, 10^9 decays of the ^{22}Na source were simulated. The maximum rate on one of the two detectors in the experiment is 11 kHz. For this rate, the probability to detect another independent particle in the time frame of the coincidence window of 2 ns is only 0.04 ‰. Therefore, we exclude pile-up effects in the simulation.

C. Coincidence Setup

The coincidence setup is described in detail in [11] and [14]. The collimator was placed between the two detectors as shown in Fig. 1. The fan-beam collimator was equipped with two ^{22}Na sources of approximately 6 MBq each. The detector under test was mounted on an electrically driven translation stage (LIMES 90, Owis, Staufen im Breisgau, Germany). The manufacturer specifies the linear stage's maximum position repetition error to 2 µm. A feedback loop allowed to control the current position of the translation stage. The whole setup was placed in a light-tight temperature chamber.

D. Radiation Detectors

We employed the Philips Digital Photon Counting (PDPC) technology evaluation kit (TEK) as readout architecture utilizing two sensor tiles equipped with digital SiPM DPC 3200-22. As the setup was only used for counting the number of gamma interactions as described in Section III-B, only the main features of the photosensor are described: the sensor tile consists of an array of 16 independent DPC 3200-22 with 4 readout channels each. Each readout channel contains 3200 single-photon avalanche diodes (SPADs) which are connected to an individual logic circuit for charging and readout. Every DPC applies a configurable two-level trigger scheme. In case the first trigger is validated by reaching the second threshold, a hit is generated. In this case, all 4 channels of the DPC, as well as a timestamp are sent to the readout architecture. To reduce dark counts of the photosensor, the DPC allows disabling the most noisiest SPADs. More detailed information can be found in [35]–[37].

For the detector under test, a high-resolution segmented LYSO array was used as in the Hyperion II^D system [38]. The scintillator array contains 900 segments of 12-mm height with 1-mm pitch leading to outer dimensions of 30 mm $\times$ 30 mm. For the coincidence detector, a one-to-one coupled LYSO scintillator of 19-mm height and outer

dimensions of 32 mm × 32 mm was employed to achieve a high coincidence rate.

III. Methods

A. Simulation Analysis

We analyzed the beam profile in two different modes. First, all gamma photons registered in the virtual planes were taken into account, so-called singles. In a second step, we considered only gamma photons where at least 100 keV were deposited in the coincidence detector. This is then referred to as coincidence events. For both cases, a profile histogram perpendicular to the slit was filled. As the profiles were box-shaped with smeared edges, first the plateau P was detected by calculating the arithmetic mean of the central bins. Then the two bins between which the desired fraction in height was passed, were identified at both edges. The full width at half maximum (FWHM) and the full width at tenth maximum (FWTM) were determined with the aid of a linear interpolation between the centers of the two identified edge bins. Uncertainties were calculated through binning variation.

The simulated beam widening was compared to pure ray optics as this defines the lower limit for the beam width. Using the intercept theorem, the widening of the beam profile can be described as

$$\frac{w}{s} = \frac{d}{c} + 1 \tag{1}$$

with w the width of the beam, s the slit width, d the distance to the collimator, and c the distance of the sources to the edge of the collimator.

To analyze the reduction of used events in the slit region by cutting on coincidences, the number of accepted gamma particles were compared. The beam profiles were integrated over the nominal slit width to have a common range for both modes and the ratio of the values of the integrals I_{singles} and I_{coinc} were calculated. The efficiency of the collimation was investigated by calculating the fractions of gamma photons inside the FWTM and the FWHM to all analyzed events. The fractions are denoted as $f_{\text{FWTM,singles}}$, $f_{\text{FWTM,coinc}}$, $f_{\text{FWHM,singles}}$, and $f_{\text{FWHM,coinc}}$. Additionally, the energy spectrum was studied. Nonscattered gamma particles of the electron-positron annihilation with the full energy of 511 keV are desired for calibration. Therefore, the fractions of gamma photons with energies in the interval 500 keV to 520 keV $f_{511\text{ keV,singles}}$ and $f_{511\text{ keV,coinc}}$ to all gammas were calculated. As they change only marginally with distance to the collimator, the average of all fractions for different distances for a given slit width is listed. To stay independent of a specific detector configuration, no energy smearing is applied and the true kinetic energy from the Monte Carlo simulation is used.

The simulation was experimentally validated with a measurement as described in Section III-B. The used LYSO crystal to count the gamma rates had a thickness of 12 mm. Assuming an absorption length of 12 mm [39] and an exponential shape of the interaction probability, the mean depth of interaction in this crystal is at 4.0 mm. Measurements were carried out with distances of 7 mm and 30 mm of the detector front face to the collimator. Thus, they were compared to the beam profile in the virtual planes at 11 mm and 34 mm.

B. Experimental Beam Characterization

The gamma photons' beam profile for slit widths of 0.4 mm and 1 mm was measured by step-wise moving the edge of the detector under study into the beam as presented in [11] and [40]. The profile $b(y)$ is given by a discrete derivative of the count rate $m(y)$ at the measurement points y_i as

$$b_i := b\left(\frac{y_i + y_{i+1}}{2}\right) = \frac{m(y_{i+1}) - m(y_i)}{y_{i+1} - y_i}. \tag{2}$$

We sampled around one edge of the detector at least for 2 mm with a step size of 50 μm. Gamma interactions were recorded for 500 s per irradiation position to achieve a low statistical error. The error of b_i was obtained by Gaussian error propagation assuming a Poisson error for the count rate and the positioning repetition error of the linear stage of 2 μm.

To determine the count rate with low noise, we set the DPCs to the highest available trigger scheme 4 requiring on average 8.33 detected optical photons to generate the first trigger. This scheme provides a high sensitivity of the photosensor as the dead time induced by dark counts is reduced. Due to the high trigger threshold, the timing performance is limited to about 1 ns coincidence resolving time [41] which is not of importance in this case. The second threshold was set to require on average 54 optical photons (scheme: 0x55:AND) [42]. Furthermore, we disabled 10% of the noisiest SPADs. Measurements were conducted at an ambient temperature of 10 °C.

All generated DPC hits need to be correlated to gamma interactions as presented in [43]. As all DPCs trigger independently, a single gamma interaction can contain up to 16 DPC hits. We employed a cluster time window of 40 ns. The time-stamp of the resulting cluster equals the timestamp of the first DPC hit. Afterward, a sliding coincidence window of 2 ns was employed. Expecting around 2000 detected optical photons for a 511 keV gamma interaction, clusters with less than 100 detected optical photons were neglected to reduce noise. The count rate $m(y)$ is calculated based on the accepted clusters; no further quality cuts were applied.

The widths of the so-obtained beam profiles was determined analogous to the simulation (see Section III-A). The uncertainties arise from the uncertainty on the plateau value.

IV. Results

A. Beam Characterization

The simulation shows that the form of the profiles is box-shaped and blurs toward the edges (see Fig. 3). The edges of the beam profiles smear out with increasing distance to the collimator [see Fig. 3(a)]. The total number of recorded gammas is reduced as the solid angle covered by the constant plane size is reduced with increasing distance. Using a larger slit increases the integral substantially [see Fig. 3(b) and Fig. 4] reducing the time needed for calibration. Longer tails are present when using singles, while they are highly reduced by using only coincidence events as shown in Fig. 3(c).

The shape of the beam profile is stable in the x-direction along the slit. However, the height of the beam profile's plateau

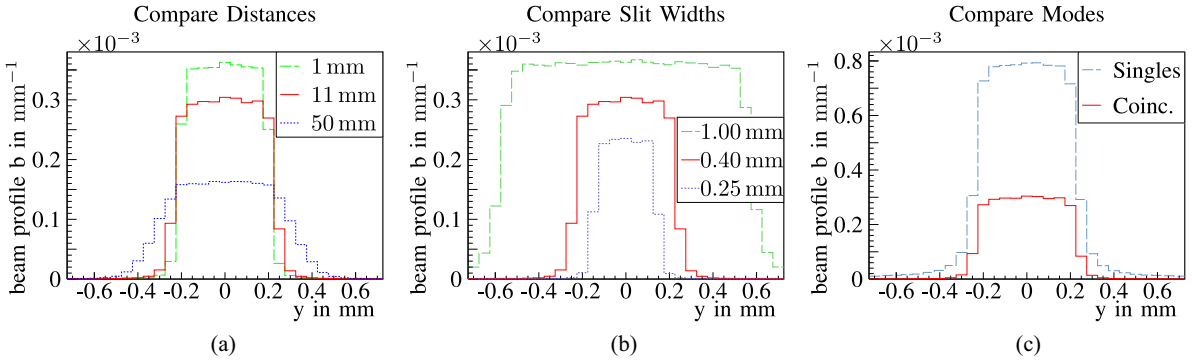

Fig. 3. Comparison of simulated beam profile histograms for different configurations normalized to the number of primary decays. (a) Profiles for coincidence events for a slit width of 0.4 mm at different distances to the collimator. (b) Profiles for coincidence events for different slit widths at a distance of 11 mm. (c) Profiles for singles and coincidence singles at a distance of 11 mm to the collimator for a slit width of 0.4 mm.

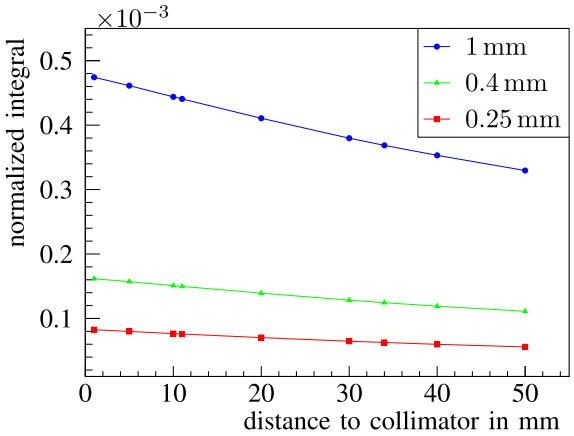

Fig. 4. Simulated number of hits on a 50 mm × 50 mm-plane normalized to the number of primary decays for slit widths of 0.25 mm, 0.4 mm, and 1 mm at different positions in front of the collimator. The relative errors are below 1% and thus not visible in the plot.

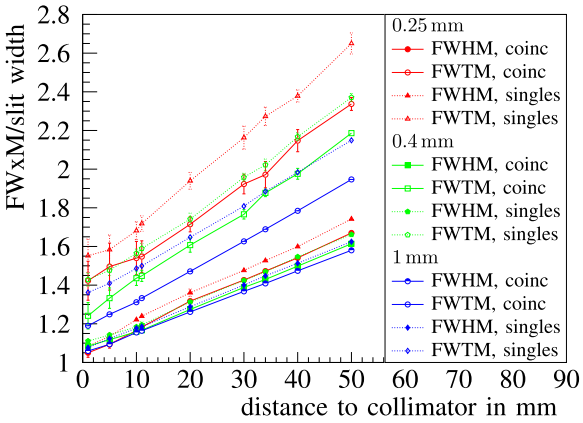

Fig. 5. Simulated FWHMs and FWTMs for slit widths of 0.25 mm, 0.4 mm, and 1 mm at different positions in front of the collimator.

degrades slightly toward the edges of the 50 mm span. Very close to the collimator, these differences can be up to 25%. From a distance of 20 mm on, the deviation is stable at values of 3% to 11% due to the different solid angle coverage further away from the source. As the count rate in the plateau region varies by a few percent also in the y-direction, this is in the same order of magnitude and does not affect the calibration.

FWHMs and FWTMs of the gamma beam for different slit widths are displayed in Fig. 5. The FWHMs are very similar for singles and coincidence events, whereas the FWTMs are larger for singles than for coincidence events indicating larger tails and background.

Taking the FWHM of the coincidence events as w the widening is up to 17% larger than the lower limit calculated from pure ray optics.

When using all singles, still a large number of gamma photons reached the detector outside the beam region and created a large background for a position-dependent calibration (see Table I). For the smallest investigated slit not even half of the accepted gamma photons were inside the FWTM of the expected beam region. Considering only coincidence events, the fraction of accepted gamma photons inside the FWHM is increased to more than 80%. Taking into account all accepted gamma photons inside the FWTM, so still very close to the desired beam position, this value rises to more than 94% giving a very clean signal. However, the number of gammas in the slit region is decreased by a factor of 2 to 3 by only using coincidence events leading to a longer calibration time (see Table II).

TABLE I
SIMULATED FRACTIONS OF GAMMAS INSIDE THE FWTM AND THE FWHM

slit width	$f_{\text{FWTM,singles}}$	$f_{\text{FWTM,coinc}}$
0.25 mm	$(48.0 \pm 2.8)\,\%$	$(94.4 \pm 1.2)\,\%$
0.40 mm	$(62.2 \pm 2.3)\,\%$	$(95.1 \pm 0.9)\,\%$
1.00 mm	$(78.3 \pm 1.3)\,\%$	$(96.0 \pm 0.4)\,\%$
slit width	$f_{\text{FWHM,singles}}$	$f_{\text{FWHM,coinc}}$
0.25 mm	$(43.0 \pm 1.9)\,\%$	$(83.7 \pm 3.8)\,\%$
0.40 mm	$(56.9 \pm 2.3)\,\%$	$(85.5 \pm 4.1)\,\%$
1.00 mm	$(72.7 \pm 0.7)\,\%$	$(92.0 \pm 1.5)\,\%$

TABLE II
COMPARISON OF THE SIMULATED INTEGRAL FOR SINGLES AND COINCIDENCE EVENTS

slit width	$I_{\text{singles}}/I_{\text{coinc}}$
0.25 mm	2.74 ± 0.04
0.40 mm	2.64 ± 0.03
1.00 mm	2.50 ± 0.03

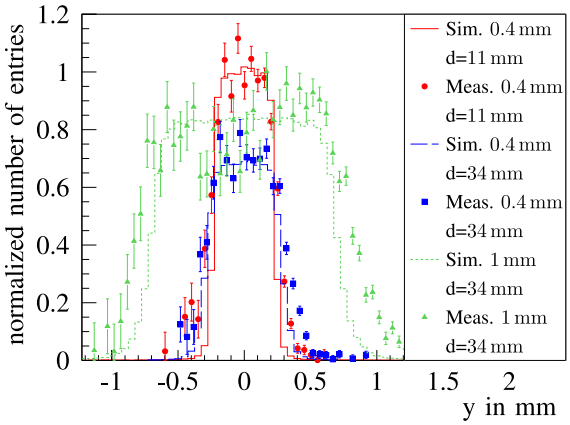

Fig. 6. Comparison of the simulated beam profile with the measurement for slit widths of 0.4 mm and 1 mm using only coincidence events.

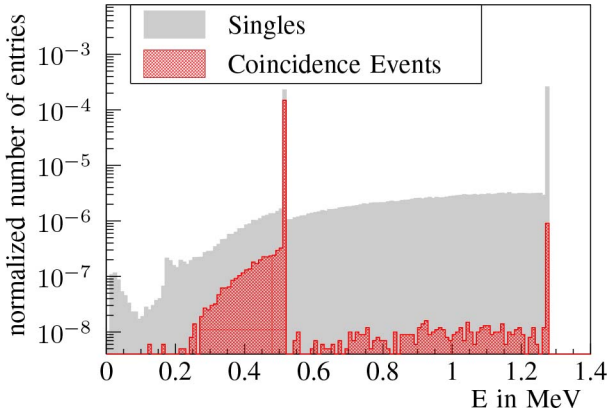

Fig. 7. Energy spectrum of simulated gammas at 1 mm in front of the collimator with a slit of 0.4 mm on a 50 mm × 50 mm plane, normalized to the number of primary decays.

TABLE III
FWHM OF SIMULATED AND MEASURED BEAM PROFILES

Slit	Distance	Simulation	Measurement
0.4 mm	11 mm	(0.467 ± 0.004) mm	(0.534 ± 0.004) mm
0.4 mm	34 mm	(0.572 ± 0.001) mm	(0.671 ± 0.004) mm
1.0 mm	34 mm	(1.409 ± 0.002) mm	(1.661 ± 0.008) mm

TABLE IV
SIMULATED RATIO OF 511 keV GAMMAS ON A DETECTOR

slit width		$f_{511\,\mathrm{keV,singles}}$	$f_{511\,\mathrm{keV,coinc}}$
0.25 mm	50 × 50	(26.3 ± 1.5) %	(96.8 ± 0.4) %
0.40 mm		(35.5 ± 1.4) %	(97.4 ± 0.3) %
1.00 mm		(46.9 ± 1.0) %	(97.6 ± 0.3) %
0.25 mm	FWHM	(55.1 ± 0.2) %	(99.4 ± 0.1) %
0.40 mm		(57.0 ± 0.2) %	(99.4 ± 0.1) %
1.00 mm		(60.6 ± 0.3) %	(99.4 ± 0.2) %

In Fig. 6, both simulated and measured beam profiles for a slit widths of 0.4 mm and 1 mm are displayed together. As not all particles are recorded in the measurement due to the limited interaction and detection probability the profiles are scaled to the same plateau value. For the measurement with a 0.4 mm slit, the profiles at the two distances are scaled with the same factors to show that simulation reproduces the same distance dependence as the measurement.

For the three compared profiles the FWHMs are noted in Table III. The measured value for the slit of 0.4 mm at a distance of 11 mm is 12% larger than the simulated one whereas both experimental values at a distance of 34 mm deviate by 15% from the simulation.

B. Energy Distribution

The energy spectrum of the simulated gamma particles leaving the collimator is shown exemplarily for the 0.4 mm slit width in Fig. 7. Taking all singles into account, the full spectrum is visible, whereas 511-keV photons are desired for calibration. Referring to the 50 mm × 50 mm plane, the fraction of 511-keV photons is less then 50% for the three investigated slits and up to about 60% taking into account only the FWHM of the beam (see Table IV). Cutting on coincidence events removes primarily gammas outside the 511-keV peak, thus increasing the fraction of 511-keV gamma particles to more than 96% on the full plane and even to more then 99% in the beam region. To get the fraction of detected gammas on a specific detector, the energy spectrum has to be folded with the energy dependent interaction probability.

V. DISCUSSION

The developed fan-beam collimator allows for a reliable and precise adjustment of the beam width utilizing the fine pitch screws and dial indicator. This allows to find the best suitable tradeoff between a fine resolution of the position and the calibration time for each application. In case discrete beam widths are sufficient, the concept could be simplified by using washers of known height to maintain the distance between shielding cakes and bottom shielding.

The simulation shows box-shaped beam profiles with a widening which is only up to 17% larger than the lower constraint given by pure ray optics. This is a pleasing result as the ray optics ignores any Compton scatter and gamma particles passing through the lead.

Restricting the gamma interactions to coincidences improves the ratio of gamma particles inside the FWTM of the beam to more than 94% while the effect is more prominent for thinner beam widths. Although loosing around one-third of all events when discarding singles, we expect a clear benefit by the clean gamma beam. A larger beam width could compensate for the longer calibration time. Also, coincidence detectors with a higher absorption efficiency can be employed. Furthermore, the energy distribution significantly improves when selecting coincidences. Additionally this suppresses background events from the internal radioactivity of LYSO, which can occur with the same rate as events from the used radioactive source. Without the selection they spoil the sample of calibration events. The particular benefit of the clean beam profile depends on the applied positioning

algorithm. Especially lazy learners like the widely used kNN suffer from noisy sets of training data and can profit from the clean data samples provided by measurements with our collimator.

The experimental determination of the beam width was able to resolve thin beams. The linear stage's step size, the accuracy of the mechanical setup and the count rate statistics limit the achievable resolution and precision. The presented method also allows to determine the edge of the scintillator crystal and calibrate the offset of the linear stage's coordinate system.

The determined FWHM of the beam differed between experiment and simulation up to 15%. We expect a wider beam profile in the experiment as the simulation does not suffer from detector effects. Most important, the measurement includes interactions along the full crystal thickness instead of a single plane. Additional effects like interactions in the outer reflector material, scattering on surrounding material or slight imperfections of the detector positioning such as a marginal tilt contribute to the smearing. Overall the agreement is satisfying. Furthermore, the height of the beam profile was found to be consistent for different distances validating the simulation.

It was reported that a few thousand events per position is a reasonable amount of training data for position estimation algorithms [32], [33]. In [33] we showed, that we need an irradiation time of 36 min to acquire 5000 events with a 0.25 mm slit on a 32 mm $\times$ 32 mm $\times$ 12 mm-monolith with a pitch of 0.75 mm to reach an FWHM of 1.42 mm in the distribution of reconstructed positions. It is even possible to decrease the number of events and accordingly the irradiation time by a factor of ten but this degrades the positioning resolution by 40%. This illustrates the short calibration times achievable with our collimator.

For slit widths in the same range as the archived positioning resolution, we see that the slit width folds into the position estimation. We found that for our specific set-up, a slit width of 0.4 mm provides a good compromise to calibrate a detector in reasonable time. A slit width of 0.25 mm could be used to validate a calibration as the fan-beam collimator provides a beam thinner than our positioning accuracy. At this point, the fast change between different slit widths of the presented collimator design is highly favorable. To the author's knowledge, the presented collimator design is the first allowing such a measurement conception.

The precise knowledge of the beam profile can be used to deconvolve the detector's point spread function, which is employed for monolithic scintillators to report the positioning performance. Thereby, positioning performance parameters, such as the spatial resolution, could be reported corrected for the finite beam size.

Currently, collimated gamma beams are mainly employed for the calibration of monolithic scintillation detectors. As recently shown, collimated gamma beams give additional insights for pixelated arrays as well [40]. A pinhole collimator was used to study general characteristics of Compton scatter for a single highly segmented crystal to identify and exclude such gamma interactions on system level. Employing a fan-beam collimator enabling time-efficient calibrations, segmented arrays could be calibrated individually to apply detector-specific positioning algorithms. Besides, the proposed fan-beam collimator concept could be of interest for calibration of different types of radiation detectors, such as Compton cameras.

VI. Conclusion

We presented an adjustable fan-beam collimator for fast calibration of monolithic scintillation detectors used for PET. The design based on standard elements makes it simple to manufacture. It features an easily and precisely adaptable slit width and is equipped with a source alignment tool which allows for convenient placement of two radioactive sources. The collimator was characterized by Geant4 simulations to evaluate the beam profile and energy spectrum. Measurements validate the results of the simulation experimentally. We found that the collimator produces beams with a flat plateau where the FWHM is less than 10% wider than the slit directly behind the collimator. The fraction of gamma photons inside the beams FWTM is larger than 94% when using a coincidence detector on the opposite site of the collimator. The setup additionally allows for an accurate selection of 511-keV gammas so that the fraction of these photons is larger than 96% on the detector plane and even more than 99% in the beam region providing optimal conditions for detector calibration. This knowledge of beam quality and shape can be employed to tailor future calibration methods.

Acknowledgment

The authors greatly thank the team of the university hospital Aachen's workshop for the manufacturing of all components.

References

[1] M. E. Phelps, *PET: Molecular Imaging and its Biological Applications*. New York, NY, USA: Springer, 2004.

[2] R. Myers, "The biological application of small animal PET imaging," *Nucl. Med. Biol.*, vol. 28, no. 5, pp. 585–593, Jul. 2001. [Online]. Available: https://www.sciencedirect.com/science/article/pii/S096980510100213X

[3] T. K. Lewellen, "The challenge of detector designs for PET," *Amer. J. Roentgenol.*, vol. 195, no. 2, pp. 301–309, 2010.

[4] P. Lecoq, "Development of new scintillators for medical applications," *Nucl. Instrum. Methods Phys. Res. A, Accelerators Spectrometers Detectors Assoc. Equip.*, vol. 809, pp. 130–139, Feb. 2016. [Online]. Available: https://www.sciencedirect.com/science/article/pii/S0168900215009754

[5] J. Cabello and S. I. Ziegler, "Advances in PET/MR instrumentation and image reconstruction," *Brit. J. Radiol.*, vol. 91, no. 1081, Jan. 2018, Art. no. 20160363. [Online]. Available: https://www.birpublications.org/doi/10.1259/bjr.20160363

[6] G. Borghi, V. Tabacchini, and D. R. Schaart, "Towards monolithic scintillator based TOF-PET systems: Practical methods for detector calibration and operation," *Phys. Med. Biol.*, vol. 61, no. 13, pp. 4904–4928, Jul. 2016. [Online]. Available: http://stacks.iop.org/0031-9155/61/i=13/a=4904?key=crossref.6f1c88b5b5a458e67275d3b7b418d509

[7] H. T. van Dam, G. Borghi, S. Seifert, and D. R. Schaart, "Sub-200 Ps CRT in monolithic scintillator PET detectors using digital SiPM arrays and maximum likelihood interaction time estimation," *Phys. Med. Biol.*, vol. 58, no. 10, pp. 3243–3257, 2013. [Online]. Available: http://www.ncbi.nlm.nih.gov/pubmed/23611889

[8] P. Bruyndonckx *et al.*, "Evaluation of machine learning algorithms for localization of photons in undivided scintillator blocks for PET detectors," *IEEE Trans. Nucl. Sci.*, vol. 55, no. 3, pp. 918–924, Jun. 2008. [Online]. Available: http://ieeexplore.ieee.org/document/4545078/

[9] R. Marcinkowski, P. Mollet, and R. V. Holen, "Sub-millimetre DOI detector based on monolithic LYSO and digital SiPM for a dedicated small-animal PET system," *Phys. Med. Biol.*, vol. 61, no. 5, pp. 1–17, 2016. [Online]. Available: http://iopscience.iop.org/article/10.1088/0031-9155/61/5/2196/meta

[10] A. J. Gonzalez *et al.*, "Initial results of the MINDView PET insert inside the 3T mMR," *IEEE Trans. Radiat. Plasma Med. Sci.*, vol. 3, no. 3, pp. 343–351, May 2019.

[11] F. Müller, D. Schug, P. Hallen, J. Grahe, and V. Schulz, "Gradient tree boosting-based positioning method for monolithic scintillator crystals in positron emission tomography," *IEEE Trans. Radiat. Plasma Med. Sci.*, vol. 2, no. 5, pp. 411–421, Sep. 2018. [Online]. Available: https://ieeexplore.ieee.org/document/8360486/

[12] M. Stockhoff, R. Van Holen, and S. Vandenberghe, "Optical simulation study on the spatial resolution of a thick monolithic PET detector," *Phys. Med. Biol.*, vol. 64, Aug. 2019, Art. no. 195003. [Online]. Available: http://iopscience.iop.org/article/10.1088/1361-6560/ab3b83

[13] X. Li, C. Lockhart, T. K. Lewellen, and R. S. Miyaoka, "A high resolution, monolithic crystal, PET/MRI detector with DOI positioning capability," in *Proc. IEEE 30th Annu. Int. Conf. Eng. Med. Biol. Soc.*, vol. 30. Vancouver, BC, Canada, 2008, pp. 2287–2290. [Online]. Available: http://www.pubmedcentral.nih.gov/articlerender.fcgi?artid=PMC2729160

[14] F. Müller, D. Schug, P. Hallen, J. Grahe, and V. Schulz, "A novel DOI positioning algorithm for monolithic scintillator crystals in PET based on gradient tree boosting," *IEEE Trans. Radiat. Plasma Med. Sci.*, vol. 3, no. 4, pp. 465–474, Jul. 2019. [Online]. Available: https://ieeexplore.ieee.org/document/8554136/

[15] Y. Wang, W. Zhu, X. Cheng, and D. Li, "3D position estimation using an artificial neural network for a continuous scintillator PET detector," *Phys. Med. Biol.*, vol. 58, no. 5, pp. 1375–1390, Mar. 2013. [Online]. Available: http://stacks.iop.org/0031-9155/58/i=5/a=1375?key=crossref.c6cd0ef8548ea88fd6d51528410c2dba

[16] I. Mohammadi, I. F. C. Castro, P. M. M. Correia, A. L. M. Silva, and J. F. C. A. Veloso, "Minimization of parallax error in positron emission tomography using depth of interaction capable detectors: Methods and apparatus," *Biomed. Phys. Eng. Exp.*, vol. 5, no. 6, Oct. 2019, Art. no. 062001. [Online]. Available: https://iopscience.iop.org/article/10.1088/2057-1976/ab4a1b

[17] G. B. Saha, *Basics of PET Imaging Basics of PET Imaging*. Cham, Switzerland: Springer, 2016.

[18] A. J. González, F. Sánchez, and J. M. Benlloch, "Organ-dedicated molecular imaging systems," *IEEE Trans. Radiat. Plasma Med. Sci.*, vol. 2, no. 5, pp. 388–403, Sep. 2018.

[19] M. Z. Pajak *et al.*, "NEMA NU4-2008 performance evaluation of albira: A two-ring small-animal PET system using continuous LYSO crystals," *Open Med. J.*, vol. 3, no. 1, pp. 12–26, Apr. 2016. [Online]. Available: https://openmedicinejournal.com/VOLUME/3/PAGE/12/

[20] S. Krishnamoorthy, E. Blankemeyer, P. Mollet, S. Surti, R. Van Holen, and J. S. Karp, "Performance evaluation of the MOLECUBES β-CUBE—A high spatial resolution and high sensitivity small animal PET scanner utilizing monolithic LYSO scintillation detectors," *Phys. Med. Biol.*, vol. 63, no. 15, Jul. 2018, Art. no. 155013. [Online]. Available: http://stacks.iop.org/0031-9155/63/i=15/a=155013?key=crossref.26fd24fdd265b886fb75c7444294b40d

[21] S. Vandenberghe, E. Mikhaylova, E. D'Hoe, P. Mollet, and J. S. Karp, "Recent developments in time-of-flight PET," *EJNMMI Phys.*, vol. 3, no. 1, p. 3, Dec. 2016. [Online]. Available: http://www.ejnmmiphys.com/content/3/1/3

[22] T. Ling, T. H. Burnett, T. K. Lewellen, and R. S. Miyaoka, "Parametric positioning of a continuous crystal PET detector with depth of interaction decoding," *Phys. Med. Biol.*, vol. 53, no. 7, pp. 1843–1863, Apr. 2008. [Online]. Available: http://stacks.iop.org/0031-9155/53/i=7/a=003?key=crossref.4473273365071f6e15ff568a53cfeb16

[23] Z. Li, M. Wedrowski, P. Bruyndonckx, and G. Vandersteen, "Nonlinear least-squares modeling of 3D interaction position in a monolithic scintillator block," *Phys. Med. Biol.*, vol. 55, no. 21, pp. 6515–6532, 2010. [Online]. Available: http://iopscience.iop.org/0031-9155/55/21/012

[24] H. T. Van Dam *et al.*, "Improved nearest neighbor methods for gamma photon interaction position determination in monolithic scintillator PET detectors," *IEEE Trans. Nucl. Sci.*, vol. 58, no. 5, pp. 2139–2147, Oct. 2011.

[25] P. Conde *et al.*, "Determination of the interaction position of gamma photons in monolithic scintillators using neural network fitting," *IEEE Trans. Nucl. Sci.*, vol. 63, no. 1, pp. 30–36, Feb. 2016.

[26] A. Iborra, A. J. G. Martínez, A. Gonzalez-Montoro, A. Bousse, and D. Visvikis, "Ensemble of neural networks for 3D position estimation in monolithic PET detectors," *Phys. Med. Biol.*, vol. 64, no. 19, Oct. 2019, Art. no. 195010. [Online]. Available: http://iopscience.iop.org/article/10.1088/1361-6560/ab3b86

[27] S. Espana, R. Marcinkowski, V. Keereman, S. Vandenberghe, and R. Van Holen, "DigiPET: Sub-millimeter spatial resolution small-animal PET imaging using thin monolithic scintillators," *Phys. Med. Biol.*, vol. 59, pp. 3405–3420, Jul. 2014. [Online]. Available: http://www.ncbi.nlm.nih.gov/pubmed/24888974

[28] M. Freire, A. Gonzalez-Montoro, F. Sanchez, J. M. Benlloch, and A. J. Gonzalez, "Calibration of gamma ray impacts in monolithic-based detectors using Voronoi diagrams," *IEEE Trans. Radiat. Plasma Med. Sci.*, vol. 4, no. 3, pp. 350–360, May 2020. [Online]. Available: https://ieeexplore.ieee.org/document/8871159/

[29] P. Bruyndonckx *et al.*, "Neural network-based position estimators for PET detectors using monolithic LSO blocks," *IEEE Trans. Nucl. Sci.*, vol. 51, no. 5, pp. 2520–2525, Oct. 2004.

[30] X. Zhang *et al.*, "Performance of long rectangular semi-monolithic scintillator PET detectors," *Med. Phys.*, vol. 46, no. 4, pp. 1608–1619, Apr. 2019. [Online]. Available: https://onlinelibrary.wiley.com/doi/abs/10.1002/mp.13432

[31] P. Peng, M. S. Judenhofer, and S. R. Cherry, "Compton PET: A layered structure PET detector with high performance," *Phys. Med. Biol.*, vol. 64, no. 10, p. 10LT01, May 2019. [Online]. Available: http://stacks.iop.org/0031-9155/64/i=10/a=10LT01?key=crossref.a236b3ff82965f28d733071c5b129306

[32] G. Borghi, V. Tabacchini, S. Seifert, and D. R. Schaart, "Experimental validation of an efficient fan-beam calibration procedure for *k*-nearest neighbor position estimation in monolithic scintillator detectors," *IEEE Trans. Nucl. Sci.*, vol. 62, no. 1, pp. 57–67, Feb. 2015. [Online]. Available: http://ieeexplore.ieee.org/document/7012118/

[33] F. Müller, D. Schug, P. Hallen, and V. Schulz, "Time-efficient calibration enabled by a gradient-tree-boosting-based positioning method for monolithic scintillators suitable for total-body PET," in *Proc. Abstracts Total Body PET Conf.*, Ghent, Belgium, Jun. 2018, p. A11.

[34] S. Agostinelli *et al.*, "Geant4—A simulation toolkit," *Nucl. Instrum. Methods Phys. Res. A, Accelerators Spectrometers Detectors Assoc. Equip.*, vol. 506, no. 3, pp. 250–303, 2003. [Online]. Available: http://www.sciencedirect.com/science/article/pii/S0168900203013688

[35] T. Frach, G. Prescher, C. Degenhardt, R. De Gruyter, A. Schmitz, and R. Ballizany, "The digital silicon photomultiplier—Principle of operation and intrinsic detector performance," in *Proc. IEEE Nucl. Sci. Symp. Conf. Rec.*, Orlando, FL, USA, 2009, pp. 1959–1965.

[36] T. Frach, G. Prescher, C. Degenhardt, and B. Zwaans, "The digital silicon photomultiplier—System architecture and performance evaluation," in *Proc. IEEE Nucl. Sci. Symp. Med. Imag. Conf.*, Knoxville, TN, USA, Oct. 2010, pp. 1722–1727. [Online]. Available: http://ieeexplore.ieee.org/document/5874069/

[37] R. Marcinkowski, S. Espana, R. Van Holen, and S. Vandenberghe, "Effects of dark counts on digital silicon photomultipliers performance," in *Proc. IEEE Nucl. Sci. Symp. Med. Imag. Conf. (NSS/MIC)*, Seoul, South Korea, Oct. 2013, pp. 1–6. [Online]. Available: http://ieeexplore.ieee.org/document/6829323/

[38] B. Weissler *et al.*, "A digital preclinical PET/MRI insert and initial results," *IEEE Trans. Med. Imag.*, vol. 34, no. 11, pp. 2258–2270, Nov. 2015. [Online]. Available: http://ieeexplore.ieee.org/lpdocs/epic03/wrapper.htm?arnumber=7097723

[39] "LYSO scintillation material," Saint-Gobain Ceramics & Plastics, Inc., Harrisburg, PA, USA, Rep., Aug. 2017. [Online]. Available: https://www.crystals.saint-gobain.com/sites/imdf.crystals.com/files/documents/lyso-material-data-sheet_0.pdf

[40] C. Ritzer, P. Hallen, D. Schug, and V. Schulz, "Intercrystal scatter rejection for pixelated PET detectors," *IEEE Trans. Radiat. Plasma Med. Sci.*, vol. 1, no. 2, pp. 191–200, Mar. 2017. [Online]. Available: http://ieeexplore.ieee.org/document/7843591/

[41] D. Schug *et al.*, "Initial PET performance evaluation of a preclinical insert for PET/MRI with digital SiPM technology," *Phys. Med. Biol.*, vol. 61, no. 7, pp. 2851–2878, Apr. 2016. [Online]. Available: http://stacks.iop.org/0031-9155/61/i=7/a=2851?key=crossref.426708d4cb33509b1f99abeada9ac877

[42] V. Tabacchini, V. Westerwoudt, G. Borghi, S. Seifert, and D. R. Schaart, "Probabilities of triggering and validation in a digital silicon photomultiplier," *J. Instrum.*, vol. 9, no. 06, 2014, Art. no. P06016.

[43] D. Schug *et al.*, "Data processing for a high resolution preclinical PET detector based on philips DPC digital SiPMs," *IEEE Trans. Nucl. Sci.*, vol. 62, no. 3, pp. 669–678, Jun. 2015.